Soft Matter

PAPER

View Article Online
View Journal | View Issue

Cite this: *Soft Matter*, 2025, 21, 7963

Comparative structural and rheological analysis of model and clinical surfactants: role of protein-enriched multilayers and bulk supply

Maria C. Novaes-Silva,[a] Mariana Rodríguez-Hakim,[b] Ainhoa Collada,[c] Benjamin R. Thompson,[d] Pablo Sanchez-Puga,[e] Kiet Pham,[d] Javier Tajuelo,[f] Philipp Gutfreund,[e] Jesús Pérez-Gil,[c] Miguel A. Rubio,[b] Norman J. Wagner[d] and Jan Vermant *[a]

Received 31st July 2025,
Accepted 22nd September 2025

DOI: 10.1039/d5sm00785b

rsc.li/soft-matter-journal

Pulmonary surfactant is essential for reducing the surface stress at the alveolar liquid–air interface, but the mechanisms leading to this reduction are still not fully understood. The occurrence of protein modulated multilayers below the interface has been reported, and they have been suggested to play a role in lung surfactant dynamics. However, evidence on their formation and their precise role in lowering the surface stress remains limited. In the present study, we combine neutron reflectometry using a Quadrotrough interfacial dilatational rheometer, with cryo-TEM imaging to investigate the conditions required for multilayer formation and their subsequent influence on interfacial properties. By comparing three model lipid systems with varying concentrations of hydrophobic surfactant proteins SP-B and SP-C, we demonstrate that a higher protein content is necessary for the formation of multilayers and the efficient re-spreading of lipids upon expansion. When comparing the model systems with the natural surfactant replacement Infasurf, we found that multilayers alone are insufficient to reduce the surface stress effectively. These results confirm that both the multilayers and the continuous bulk lipid–protein supply play a critical role in efficiently achieving a low surface stress through structural modifications.

Introduction

Pulmonary surfactant (PS) is a complex mixture of lipids and proteins synthesized by type II alveolar cells that reduces breathing effort and prevents alveolar collapse upon exhalation.[1,2] Phospholipids comprise the largest percentage of this mixture (∼80 wt%), followed by neutral lipids (∼10 wt%) and surfactant proteins (SP, ∼8 wt%).[3,4] Although present in small amounts (∼1 wt%), the hydrophobic proteins SP-B and SP-C fulfill essential biophysical roles such as forming lamellar bodies (LBs) for PS storage and secretion,[5] accelerating surfactant adsorption at the air–liquid alveolar interface,[1,6,7] improving interfacial film stability,[8,9] and facilitating respreading.[4,10] These functions are so vital that SP-C and SP-B deficiency in mice leads to chronic respiratory failure and lethal respiratory failure at birth, respectively.[10,11]

Most protein functions have been associated with their ability to interact with lipid bilayers, affecting their structure.[4,12] SP-B dimers have been shown to form ring-shaped oligomers, creating parallel interactions between two membrane surfaces.[13] The internal part of this ring is claimed to be hydrophobic, enabling lipid exchange between the interconnected membranes. This is particularly relevant for interfacial film formation and stabilization, as it allows LB-like aggregates to unravel at the interface.[14,15] In addition, the strong cohesion between membranes due to lipid–protein and protein–protein interactions would allow the creation of multilayered interfacial films, which could enhance mechanical stability and facilitate surfactant recycling.[11] In Fig. 1, we illustrate the LB-like aggregates together with the multilayered interfacial structures and their organization at the alveolar air–liquid interface.

Although the role of multilayered interfacial films in lung function and stability is evident, it remains unclear whether these interfacial structures spontaneously form upon adsorption or are generated on demand in response to compression.

---

[a] *Department of Materials, ETH Zürich, CH-8093 Zürich, Switzerland. E-mail: jan.vermant@mat.ethz.ch*
[b] *Departamento de Física Fundamental, Universidad Nacional de Educación a Distancia, E28232 Madrid, Spain*
[c] *Department of Biochemistry and Molecular Biology, Faculty of Biology, and Research Institute "Hospital 12 de Octubre (imas12)", 28040 Madrid, Spain*
[d] *Chemical and Biomolecular Engineering Department, University of Delaware, Newark 19716, USA*
[e] *Institut Laue-Langevin, 38042 Grenoble, France*
[f] *Departamento de Física Interdisciplinar, Universidad Nacional de Educación a Distancia, E28232 Madrid, Spain*

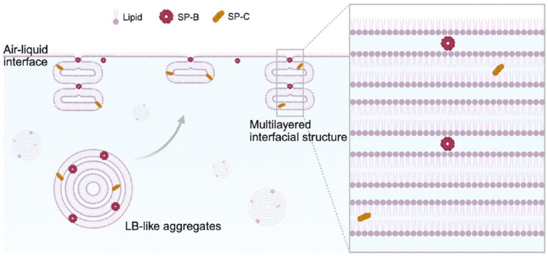

Fig. 1 Lamellar body (LB)-like aggregates, composed of dense stacks of lipid bilayers with associated proteins, unravel at the air–water interface with the aid of surfactant proteins B and C (SP-B and SP-C). This process gives rise to multilayered interfacial structures that coexist with a monolayer. The zoom-out illustrates these multilayered structures in a bilayer organization, highlighting the positions of the proteins within the lipid membranes. This schematic representation is not drawn to scale and is intended only for illustrative purposes. Based on the illustration of Castillo-Sánchez *et al.*[11] Created in BioRender. Novaes Silva, M. (2025) **https://BioRender.com/hxn8d04**.

The latter process, also known as squeeze-out, is mostly accepted.[11,16–20] This theory suggests that unsaturated lipids are expelled from the interface during compression, leading to the formation of multilayers beneath it. This mechanism would reduce surface tension by enriching the monolayer with saturated lipids, which can better withstand high surface pressures. Upon re-expansion, these lipids would be reincorporated into the monolayer.[18–20] This theory has rightfully been questioned, since most studies have been conducted at room temperature and on slowly compressed spread films.[21] Moreover, a surface tension framework captures only the equilibrium thermodynamic response.[22–24] For PS systems, a dense interface with a path-dependent response (*i.e.* dependent on strain and strain rate) is expected.[24] In this case, the total surface stress, defined as

$$\boldsymbol{\sigma} = \sigma_{\alpha\beta}(\Gamma, T)\boldsymbol{I}_{\mathbf{s}} + \boldsymbol{\sigma}_{\mathbf{e}}, \qquad (1)$$

must instead be considered. This framework accounts, not only for the equilibrium thermodynamic contribution ($\sigma_{\alpha\beta}(\Gamma,T)$), but also for rheological properties of the interface ($\boldsymbol{\sigma}_{\mathbf{e}}$).

More recently, a new theory based on adsorption-induced squeeze-out was proposed. In this case, the adsorption of bulk aggregates would directly create an interface enriched with saturated lipids, while unsaturated lipids would form multilayers.[21,25] However, this model also faces strong objections. First, evidence suggests that SP-B and SP-C primarily reside in the liquid-disordered phase and preferentially interact with anionic lipids, raising questions about this specific protein-mediated DPPC transport.[11,26,27] Second, the mechanism by which unsaturated lipids would be selectively excluded from the interface remains unclear, since a total enrichment of DPPC is neither physiologically realistic nor seems to be necessary to achieve the observed low surface tension values.[28–30] Finally, the proposed exposure of acyl chains to water during bilayer collapse appears unlikely, further challenging the validity of this model.[21] While the importance of interfacial multilayer structures is well established, the conditions required for their formation and the underlying driving mechanisms remain unclear. This uncertainty also extends to the localization of SP-B and SP-C. Evidence suggests that SP-B preferentially resides on the membrane surface, while SP-C aligns along the hydrophobic membrane core.[31] However, how these proteins are organized within multilayer structures remains unknown. Recent work using neutron reflectometry at air–liquid interfaces in conventional surface balances has determined that SP-B could be the crucial protein to establish interface-associated bilayer reservoirs.[32] However, these experiments were carried out under limiting conditions of temperature, surface pressure, and compression rates.

To elucidate the mechanisms driving interfacial multilayer formation and the role of hydrophobic proteins, we analyzed neutron reflectivity profiles of three model lipid systems with varying protein concentrations under physiologically relevant conditions. These findings were further validated using cryo-TEM imaging and benchmarked against a clinical lung surfactant formulation consisting of a full mixture of surfactant lipids and hydrophobic proteins obtained from animal lungs and currently used in surfactant replacement therapies. Our results show that multilayer structures form at high protein concentrations, indicating localized protein accumulation at the interface in physiological systems. By employing contrast variation techniques, we pinpointed the spatial distribution of proteins within the multilayers, corroborating previous molecular dynamics simulations. These results suggest that a higher protein concentration and adsorption can induce multilayer formation, and that the mere presence of multilayers at the interface is not sufficient to significantly reduce surface stress, consistent with reports highlighting the importance of sighing and non-equilibrium mechanical responses.[24]

Materials and methods

Materials

Model systems were used as simplified representations of PS. Three different compositions were tested: (i) a lipid mixture reflecting the basic composition of natural surfactant, consisting of dipalmitoylphosphatidylcholine (DPPC), palmitoyloleoylphosphatidylcholine (POPC) and palmitoyloleoylphosphatidylglycerol (POPG) at a weight ratio of 55 : 28 : 17, (ii) the same lipid mixture supplemented with 1% (w/w) of each of the surfactant proteins SP-B and SP-C, mimicking the physiological composition, and (iii) the same lipid mixture with 10% (w/w) of SP-B and SP-C, to assess the effect of increased protein concentration. Samples were purified from surfactant complex pellets isolated from porcine bronchoalveolar lavage fluid subjected to organic extraction. Detailed purification procedures are described elsewhere.[14,33] Lipid tails in these model systems were either hydrogenated (hereafter referred to as hLip) or deuterated (hereafter referred to as dLip). All three compositions were dispersed in chloroform at a lipid concentration of 1 mM. In addition to the model systems, an exogenous surfactant replacement, Infasurf (ONY Biotech) was used as a complete PS mimic. For the subphase, we used D_2O or air contrast matched water (ACMW) buffers, containing 5 mM Trizma base and 150 mM NaCl at pH = 7.

Methods

Neutron reflectometry. A custom-made Quadrotrough designed for neutron reflectivity experiments was employed, as described by Tein *et al.*[34] It comprises a circular Teflon trough, where the subphase is placed; four motorized fingers surrounded by an elastic band, where the interface is contained; and a Wilhelmy rod coupled to a force balance to measure the surface stress (see Fig. 2B). By radially displacing the fingers, the interfacial area is compressed or expanded while maintaining its shape, to ensure a pure dilatational deformation and avoid shear effects. This feature is particularly important for phospholipids, which are known to exhibit sensitivity to interfacial shear history.[35,36] For a purely isotropic deformation, eqn (1) simplifies to $\boldsymbol{\sigma} = [\sigma_{\alpha\beta}(\Gamma,T) + \sigma_{\mathrm{e}}^{\mathrm{iso}}]\boldsymbol{I}_{\mathbf{s}}$ and the surface stress is reduced to a scalar, where $\sigma_{\alpha\beta}$ is a tension and $\sigma_{\mathrm{e}}^{\mathrm{iso}}$ can be compressive or dilatational. A custom-manufactured fluoropolymer neutron-transparent elastic band was used, with additional specifications detailed in Alicke *et al.*[22] The interfacial confinement by the elastic band is also important in preventing the leakage of surface-active molecules at the higher surface pressures. The Quadrotrough was heated to keep the subphase at 36.5 °C. To maintain both interfacial and ambient temperature at this desired value, the apparatus was kept inside a humidified PMMA chamber. This prevented liquid evaporation and suppressed evaporative cooling. A heated reservoir of either D_2O or ACMW was used to humidify the ambient environment. The Quadrotrough was installed on the FIGARO neutron time-of-flight reflectometer at the Institut Laue-Langevin (ILL).[37] Coupling the Quadrotrough with FIGARO allows the generation of interfaces compressed under physiologically relevant conditions, enabling *in situ* structural determination and the simultaneous acquisition of the surface stress.

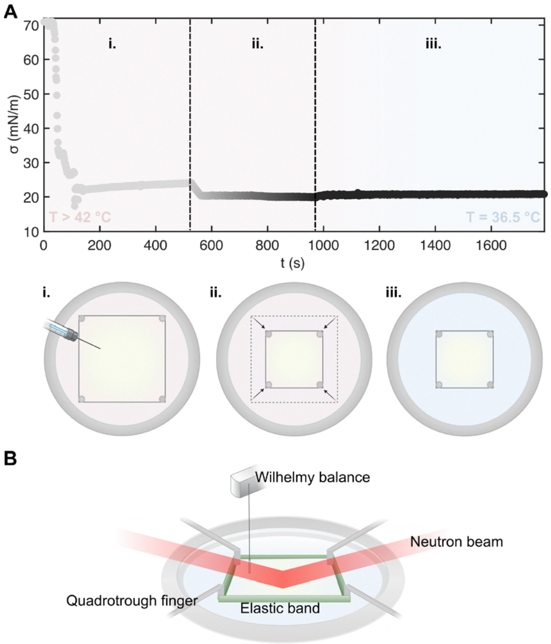

Fig. 2 Creating relevant model lipid system interfaces: (A) surface stress (σ) as a function of time (t) during different steps of the interface preparation protocol: (i) a clean buffer–air interface is maintained at $T > 42$ °C, illustrated by the light pink background. 100 μL of the desired sample (1 mM) is spread inside the square region contained inside the elastic bands (yellow background), with a total area of $A_{\mathrm{max}} = 17\,112.5$ mm^2. A ∼5 minute waiting period is included for chloroform evaporation; (ii) the interface is isotropically compressed until $A_0 = 9821$ mm^2. The compression is illustrated by the gray-to-black color gradient in the plot, where light gray represents A_{max} and black, A_0. The compression is applied quasi-statically, at a velocity of 3 mm min^{-1}, to suppress the appearance of interfacial mechanical stresses and maintain an equilibrium configuration. (iii) The temperature is reduced to 36.5 °C, illustrated by the blue background, and neutron data is acquired for a total counting time of 30 minutes. (B) Illustration of the experimental setup showing the Quadrotrough containing the desired solution. An elastic band surrounds the interfacial area of interest, whose surface stress is measured using a Wilhelmy balance and rod. For *in situ* structural analysis, the Quadrotrough is positioned inside the FIGARO neutron beamline at the ILL, such that the incident neutron beam is reflected on the interface. Illustrations created in BioRender. Novaes Silva, M. (2025) **https://BioRender.com/6nrj1iz**.

To create homogeneous and reproducible initial conditions with the model systems, we prepared the interfaces using a thermal protocol as in Hermans and Vermant.[36] This protocol is illustrated in Fig. 2A. We first set the interface temperature to $T > 42$ °C, above the melting temperature of DPPC. This higher temperature is illustrated by the light pink background. Then, on this clean D_2O or ACMW buffer–air interface, we spread 100 μL of the desired model system solution (represented by the yellow background) and waited approximately 5 minutes to allow for chloroform evaporation (step (i) in Fig. 2A). This was followed by a quasi-static isotropic compression of the interface, from $A_{\mathrm{max}} = 17\,112.5$ mm^2 to $A_0 = 9821$ mm^2 at 3 mm min^{-1} (step (ii) in Fig. 2A). The final lipid concentration at A_0 was 0.01 mmol m^{-2}. During this step, we monitor the surface stress (σ) to ensure that no rheological stresses have accumulated at the interface, such that A_0 represents the initial unstrained reference state. Once the compression was finished, we lowered the temperature to 36.5 °C, represented in the illustration by the blue background (step (iii) in Fig. 2A). Including this compression step enabled the use of a smaller spreading volume while still achieving relevant surface stresses. This is advantageous as spreading large solution volumes in small interfacial areas can promote aggregate formation and cause surface-active species to detach from the interface, leading to out-of-equilibrium configurations. Therefore, this protocol allowed us to reach relevant surface tensions, while still keeping the interface at a rheologically unstrained state. At the end of this thermal protocol, all systems had an initial surface tension of ∼25 mN m^{-1}, corresponding to the equilibrium surface tension of the phospholipid and PS systems.[23]

Following the thermal protocol, neutron data was collected at an incident angle of 3.878° using wavelengths ranging from 2 to 30 Å, maintaining a fixed momentum transfer (Q) resolution of 7%. Data was collected in 5-seconds bins over a 15 or 30-minute period. This specific combination of angle and wavelength range was chosen to optimize coverage while ensuring adequate time resolution.[38] An illustration of the main components of the experimental setup is shown in Fig. 2B.

The detected signal was processed and reduced using COSMOS.[39] Absolute reflectivity was determined by normalizing the measured signal with direct beam measurements *via* COSMOS.

Two experimental protocols were used for Infasurf. In the first, an aqueous Infasurf solution was spread directly at the buffer–air interface at 36.5 °C, with A_0 = 9821 mm^2 (hereafter referred to as Infasurf Spr.). The spreading volume was adjusted to achieve a lipid interfacial concentration of ∼0.01 mmol m^{-2}, matching that of the model systems post-compression (step (ii)). In the second protocol, a diluted Infasurf solution containing 0.5 mg of phospholipids (PL) per mL was used as the subphase, whose temperature was also maintained at 36.5 °C (hereafter referred to as Infasurf Ads.). Unlike the model lipid systems, interfaces formed with Infasurf were not subjected to the thermal protocol, in order to preserve the natural suspension aggregates and avoid alterations in solubility and adsorption, as this sample was dispersed in an aqueous buffer. Neutron data acquisition at A_0 = 9821 mm^2 followed the same protocol as the model system experiments.

To investigate the relationship between surface stress and structure, we also collected neutron data following a controlled breathing protocol. The full experiment began with a 30-minute unstrained resting period, followed by 10 cycles of tidal breathing. During each tidal breathing cycle, five complete oscillations are applied, simulating an inhalation and exhalation movement. During inhalation, the interface area is increased by 5–10% by moving the fingers at a rate of 123.6 mm min^{-1}, followed by exhalation back to A_0 at the same rate. Thus, the frequency of each inhalation–exhalation cycle is 0.3 Hz, which is equivalent to ∼18 breaths per min, which lies within physiological breathing values.[40] After the five inhalation–exhalation movements, the interface is left undisturbed for a 3-minute period, during which neutron acquisition is performed. Subsequently, 10 additional breathing cycles were conducted, this time incorporating physiologically-relevant sighing maneuvers. Thus, each cycle comprises of four tidal breathing oscillations followed by a single, larger sigh oscillation in which the interfacial area is increased by 38.5%, followed by exhalation back to A_0 both at the same rate. After the five inhalation–exhalation movements, the interface is once again left undisturbed during the 3-minute neutron acquisition period. It is worth highlighting that the choice to apply an area expansion followed by re-compression to the same initial area mimics physiologically relevant deformations. As previously reported, the lungs expand primarily rather than compress.[41] Unless otherwise specified, all neutron data refer to the initial unstrained period. For the breathing protocol, data correspond to an average of the last five breathing (+ sigh) cycles.

Measurements of the air–D$_2$O interface were performed over a broader angular range to capture the critical edge (*i.e.*, momentum transfer below which total reflection occurs) and determine the scattering length density (SLD) of the subphase. Since the goal of this study was to determine the conditions for multilayer formation, neutron data analysis was performed using a multilayer slab model with the Refl1D software package.[42] Three types of slabs were defined: (i) lipid headgroups (LH), (ii) lipid tailgroups (LT), and (iii) proteins (P). We assumed that lipids cover the interface, while structures beneath it are heterogeneously distributed. To account for this, each slab was assigned a volume fraction relative to the D$_2$O or ACMW buffer, allowing for variation in the scattering length density (SLD) along different depths. To maintain physical consistency in the model, we introduced a proportionality parameter (n = 1) linking the volume fraction (ν_f) of lipid headgroups to that of the tails. At the interface, slabs were arranged with lipid tails facing the air and headgroups embedded in the buffer. Below the interface, we defined four bilayer structures since our goal is to determine multilayer formation. Since molecular dynamics (MD) studies suggest that the hydrophobic proteins SP-C and SP-B are mainly located within the hydrophobic tail region and associate with the headgroup region,[26,31] we defined two types of protein (P) slabs: one type right after a lipid headgroup (P-HL), and the other in between the lipid tailgroups (P-Bet). Therefore, each bilayer structure is organized as: P-HL, followed by LH, LT, P-Bet, LT and, lastly, LH. The protein slabs also had an associated ν_f, however, to decrease the number of fitting parameters, we defined the proportionality parameters a and b to link $\nu_f^{\text{P-HL}}$ and $\nu_f^{\text{P-Bet}}$ to ν_f^{LH}, respectively. The thickness h of P-HL and P-Bet were allowed to vary within physically relevant ranges, namely, 10–25 Å and 0–5 Å.[27,43] For the lipid mixture system, the four bilayer structures below the interface were maintained, but without the protein slabs. Since we expect the multilayers to be more densely packed beneath the interface in some systems than in others, we allowed ν_f^{LH} of each bilayer to vary, changing consequently, ν_f^{LT}, $\nu_f^{\text{P-HL}}$ and $\nu_f^{\text{P-Bet}}$.

This model was fit to the neutron data using the DREAM algorithm.[44] Reflectivity calculations were carried out using the Abeles matrix method. Model fitting incorporated a Bayesian framework to estimate parameter uncertainties, employing Markov chain Monte Carlo (MCMC) methods to sample the joint probability distribution and derive individual parameter distributions.[44]

The model parameters for all systems, as well as a sketch illustrating the slabs are shown in the SI. Uncertainty plots obtained by the DREAM algorithm are reported in the SI and other files related to the MCMC output are available in the data repository (**https://doi.org/10.3929/ethz-b-000743121**).

Cryo-TEM. Cryogenic transmission electron microscopy (cryo-TEM) is a powerful technique for imaging lipid vesicles in their native hydrated state with nanometer-scale resolution. In this method, a thin film of the vesicle suspension is rapidly vitrified by plunging it into liquid ethane, preserving the sample without artifacts from dehydration or staining. The vitrified sample is then imaged under an electron microscope at cryogenic temperatures, allowing visualization of the size, morphology, lamellarity, and structural integrity of the vesicle.[45]

We imaged a model system composed of the lipid mixture both with and without 1% SP-C. Although vesicles containing SP-B were also imaged, their visualization was not optimal for quantitative analysis. We attribute this to SP-B's strong ability to promote adsorption,[31] which likely prevented the vesicles from being embedded within the thin film of vitreous ice.[46] In addition, SP-B has been claimed to promote aggregation and fusion of membranes to form large complexes that are difficult to confine into the thin vitreous ice film.[9] Representative images are provided in the SI. To prepare the model lipid samples, a 10 mg mL^{-1} lipid solution in chloroform was prepared, and 10 μL of it was left to evaporate overnight to remove the chloroform. The samples were then placed under vacuum for two hours to eliminate any residual solvent. Just before freezing, the dried lipid film was rehydrated in 50 μL PBS buffer (Gibco, pH 7.4) and vortexed to ensure proper dispersion. Approximately 3 μL of each sample was deposited on a Cu-300 mesh Lacey + 2 nm copper grid (Quantifoil) and immediately frozen in liquid ethane. The imaging was performed in a Titan Krios FEG (Thermo Fisher Scientific) with a dose of 50 electrons per Å^2 with a magnification of 59 000× or 96 000×. To quantify bilayer thickness, image post-processing was performed in MATLAB using a Gaussian smoothing kernel with a standard deviation of 10, followed by background subtraction. For each bilayer, a smoothed intensity profile was generated at three different locations, with the thickness defined as the distance between the two intensity minima.

Results and discussion

Structure of a lipid mixture system

To determine the structural differences between model systems with and without proteins, we first studied the neutron reflectivity of a pure lipid mixture, using three different contrasts (hLip in D_2O, dLip in D_2O, and dLip in ACMW). The results are reported in Fig. 3.

By fitting the model to the specular reflectivity data in Fig. 3A, we obtained the scattering length density (SLD) profile shown in Fig. 3B. In this profile, the layer thickness is defined with $z_{\max}$ at the buffer–air interface and $z = 0$ in the bulk. The SLD values for the different components are as listed in Table 1:

As shown in Fig. 3B, the SLD profile indicates that the interface is fully covered by lipids, with the hydrophobic tails oriented towards the air and the hydrophilic headgroups embedded in the aqueous subphase. Both the SLD profile and the fitted parameters reported in the SI indicate a negligible amount of lipids present below the interface, suggesting no prominent multilayer structure. This is expected for a pure lipid system since none of the components should stabilize multilayer structures. Instead, a packed lipid monolayer can collapse upon compression. As previously described by molecular dynamics (MD) simulations, this collapse can proceed through vesicle formation (budding[47]) when higher amounts of unsaturated lipids are used or at higher temperatures.[48] Both parameters tune the bending modulus, which was reported to vary between 0.6–1.4 × 10^{-19} J for lipid bilayers,[48,49] facilitating vesicle formation when the modulus is reduced. These conditions are attained in our system, as POPG and POPC are unsaturated lipids and experiments are performed at 36.5 °C; however, we expect a low number of vesicles to be formed. Therefore, modeling scarce structures that are detached from the top monolayer at an indefinite distance is a non-trivial endeavor. A simplified model that considers vesicles below the interface at a fixed distance captures the reflectivity curve with higher accuracy and is reported in the SI. However, this simplified model does not account for height fluctuations and vesicle polydispersity. Since the main focus of this study is to determine the conditions of multilayer formation, we kept the multilayer slab model and neglected vesicle formation, as they do not seem to impact significantly the obtained structure.

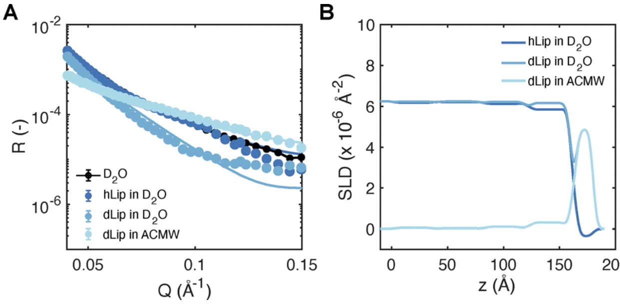

Fig. 3 Structure of a lipid mixture: (A) specular neutron reflectivity (R) as a function of momentum transfer vector (Q) for hLip in D_2O, dLip in D_2O, and dLip in ACMW at 36.5 °C. The reflectivity curve for pure D_2O is shown in black. Solid lines represent the multilayer slab model fit. (B) Scattering length density (SLD) profile obtained by the model fit, where the layer thickness (z) extends from the buffer–air interface (at $z_{\max}$) to the bulk (at z = 0).

These results confirm that, in the absence of surfactant proteins, the lipid mixture forms a stable monolayer with negligible multilayer content under physiologically relevant conditions. This system thus provides a well-defined baseline to evaluate how protein incorporation alters interfacial architecture and promotes multilayer formation.

Adding physiological amounts of proteins

To determine the effect of physiological amounts of SPs, we performed neutron reflectivity experiments using a lipid mixture with 1% SP-B and 1% SP-C. The results are shown in Fig. 4.

The reflectivity curves for the lipid mixtures with 1% proteins (Fig. 4A) closely resemble those of the pure lipid system, with only clear differences observed at the intermediate scattering of $Q \sim 0.07$ Å^{-1}, which was increased relative to the pure lipid system. We can infer from the obtained SLD profile (Fig. 4B) that the overall structure is similar to that of the pure lipid system, namely, a monolayer-dominated structure. A small amount of lipids can be inferred from the SLD profile beneath the top monolayer. While a model including bulk

Table 1 Typical SLD values for the different components in our model lipid systems and in PS

Component	SLD ($\times 10^{-6}$ Å^{-2})
Lipid headgroups	2
h-Lipid tailgroups	−0.35
d-Lipid tailgroups	4.9
SPs in D_2O	2.5
SPs in ACMW	1.5
D_2O	6.26
ACMW	0

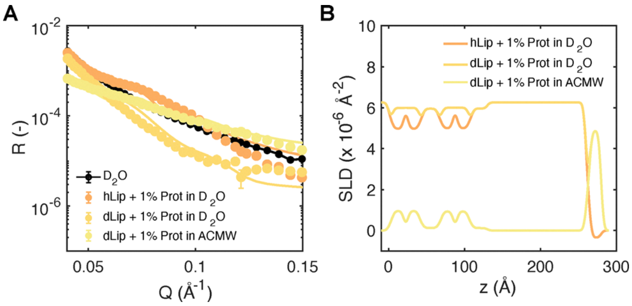

Fig. 4 The effect of physiological amounts of SPs: (A) specular neutron reflectivity (*R*) as a function of momentum transfer vector (*Q*) for hLip + 1% SP-B + 1% SP-C in D_2O, dLip + 1% SP-B + 1% SP-C in D_2O, and dLip + 1% SP-B + 1% SP-C in ACMW at 36.5 °C. The pure D_2O reflectivity curve is shown in black. Solid lines correspond to the multilayer slab model fit. (B) Scattering length density (SLD) profile obtained by the model fit, where the layer thickness (*z*) extends from the buffer–air interface (z_{max}) to the bulk (*z* = 0).

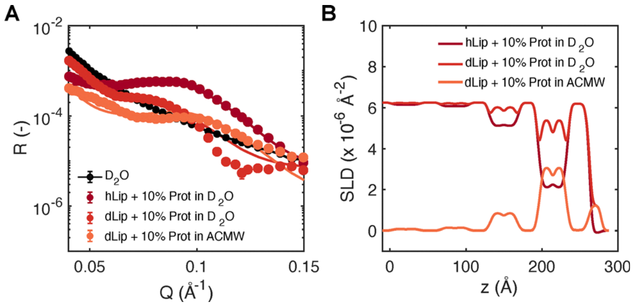

Fig. 5 Increasing protein concentration leads to multilayer formation: (A) specular neutron reflectivity (*R*) as a function of momentum transfer vector (*Q*) for hLip + 10% SP-B + 10% SP-C in D_2O, dLip + 10% SP-B + 10% SP-C in D_2O, and dLip + 10% SP-B + 10% SP-C in ACMW at 36.5 °C. The pure D_2O reflectivity curve is shown in black. Solid lines represent the multilayer slab model fit. (B) Scattering length density (SLD) profile obtained from the model fit, where the layer thickness (*z*) extends from the buffer–air interface (z_{max}) to the bulk (*z* = 0).

vesicles at larger distances, similar to that used for the lipid mixture, provides a slightly improved fit, the accuracy is insufficient to allow for reliable quantitative conclusions. Given that the lipid ν_f accounts for less than 20% in both models and that these structures do not seem to be directly attached to the monolayer, we believe that this system does not create a multilayer structure. This observation is further corroborated by the reflectivity curve, which lacks a pronounced Bragg peak, typically indicative of an ordered multilayer structure.[38]

The effect of increasing protein concentration

The presence of 1% SPs does not appear to create a notable multilayer structure under the studied conditions. Previous studies claimed that an increasing proportion of SP-B and SP-C proteins accumulate in defined regions of surface films subjected to compression–expansion dynamics, which could be relevant to modulate interfacial properties.[50,51] Therefore, we investigated the model lipid mixture with 10% SP-B and 10% SP-C. The results obtained from the neutron reflectivity experiments are shown in Fig. 5.

Qualitatively, the reflectivity curves for the 10% protein-enriched system show significant differences compared to the pure lipid system and the lipid + 1% SPs system (Fig. 5A). A broad peak appears at *Q* between ∼0.08 and ∼0.14 Å^{-1}, which is characteristic of multilayers.[38] The SLD profile obtained by the model fit (Fig. 5B) indicates a more lipid-dense architecture than that of the 1% SP, achieving a volume fraction of around 60% of lipids in the first bilayer. Another key feature is that the bilayer structures seem more closely attached to the top monolayer. Both the reflectivity curve and the SLD profile suggest that a multilayer is formed below the interface.

The SLD profiles of both protein-enriched systems provide information on the approximate location and length scale of the proteins. The inferred distributions suggest that the proteins are situated near the lipid headgroups and within the bilayer tail region. This observation is consistent with previous MD studies, which indicate that SP-C predominantly resides within the hydrophobic tail region, whereas SP-B is more likely to associate with the headgroup region.[26,31] We note, however, that the contrasts used in our study do not allow us to distinguish between the two proteins. In addition, our neutron reflectivity model fits suggest the presence of denser and thicker bilayers as SPs are added. To validate the physical relevance of these results, we performed a direct visualization of our model system vesicles with cryo-TEM imaging, as shown in Fig. 6. Although these are bulk structures, we believe that they capture relevant lipid–protein length scales for both systems, translatable for the multilayer bilayers.

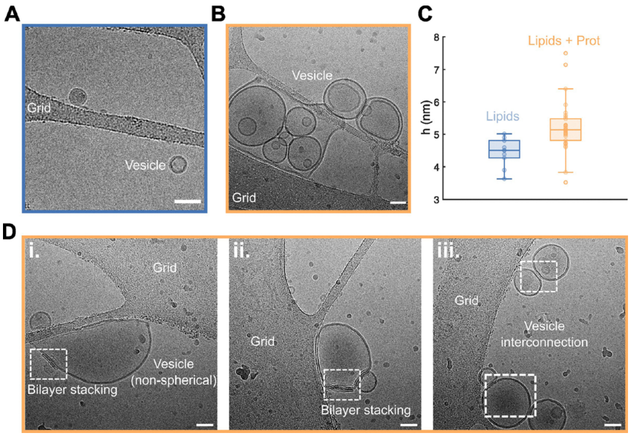

Fig. 6 Direct vesicle visualization: (A) cryo-TEM image of vesicles formed within the lipid mixture (no proteins), acquired at 59 000× magnification. (B) Cryo-TEM image of vesicles formed within the lipid mixture + 1% SP-C, with a 59 000× magnification. Both scale bars are 50 nm. (C) Bilayer thickness for the lipid mixture (blue) and lipid mixture + 1% SP-C samples (orange). A total of 10 and 30 vesicles were averaged for the lipid mixture and lipid mixture + 1% SP-C samples, respectively. The central horizontal line represents the median value, while the upper and bottom lines indicate the upper and lower quartiles, respectively. The vertical lines represent the maximum and minimum attained values not considered outliers, and the circles represent mean individual bilayer thicknesses. Circles outside the vertical lines are outliers. (D) Additional cryo-TEM images of vesicles formed with the lipid mixture + 1% SP-C, at a 59 000× magnification, illustrating how proteins tune vesicle structure: (i) non-spherical vesicle, (ii) bilayer stacking, (iii) vesicle interconnection. Scale bars are 50 nm.

A qualitative comparison between the vesicles of the lipid-only system (Fig. 6A) and those with added protein (Fig. 6B) shows that the inclusion of proteins markedly increases vesicle complexity. Fig. 6D specifically illustrates the different effects SPs can have on lipid vesicles. First, the proteins can drive vesicles away from their usual spherical shape, creating distortion (Fig. 6D(i) and (ii)), which confirms the suggested role of SPs in facilitating membrane curvature.[11] Moreover, SPs can promote interconnection of vesicles, driven by membrane–membrane contact (Fig. 6D(ii) and (iii)).[10] Lastly, there is an increased bilayer thickness.[31] A similar effect was also observed with SP-B by Bernardino de la Serna *et al.*[9] By averaging the membrane size of 30 vesicles, we obtained a bilayer thickness of 5.2 ± 0.8 nm (individual values are reported in the SI). We report the measured bilayer thickness values (h) for both the lipid-only system and the system with added protein in Fig. 6C. The length scales observed in the cryo-TEM images are consistent with those obtained with the model fitting of our neutron reflectivity data of both the 1% and 10% proteins systems (around 6 nm for bilayer), validating our observations.

All three model systems studied so far were spread from chloroform solutions at identical amounts and concentrations, yet the 10% SP solution is the only one to exhibit multilayer formation. This suggests that the interfacially-tethered multilayers arise from the higher protein content, not from simple adsorption as previously suggested.[25] Because the lipid protocol includes a quasi-static compression step, we do not yet know whether the slow compression is also necessary for driving multilayer formation. Likewise, the physiological relevance of the elevated SP concentrations remains unresolved.

These results indicate that physiological levels of surfactant proteins (1%) are insufficient to promote the formation of stable interfacial multilayers, highlighting the need to explore whether higher protein content is required to induce such structures under physiologically relevant conditions.

Comparing the model systems with a relevant PS

To address these questions, we compared the model systems with the clinical surfactant replacement Infasurf. This formulation consists of a suspension of the full lipid components plus the hydrophobic proteins SP-B and SP-C contained in native surfactant obtained from bovine bronchoalveolar lavage.[52] Neutron reflectivity measurements of the Infasurf interface were conducted using two protocols, as previously outlined. In the first, the aqueous solution was directly spread at the interface at a total interfacial concentration matching that of the model systems (Infasurf Spr.). In the second, a diluted Infasurf solution (0.5 mg PL per mL) in D_2O was used as the subphase to mimic a more physiological adsorption pathway, albeit at a lower bulk lipid concentration. The SLD profiles obtained from the model fit are shown in Fig. 7B; full reflectivity curves are provided in the SI. It is worth noting that, for both Infasurf experiments, only one contrast was used. Therefore, even if we use the same model for consistency, the location and length scale of the proteins should be carefully interpreted, since both the lipid headgroups and proteins have a SLD close to 2×10^{-6} Å^{-2}.

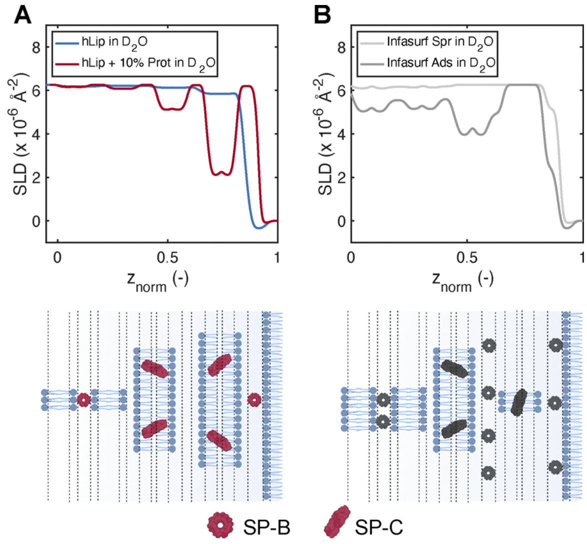

Fig. 7 Comparing the model systems with the clinical surfactant replacement Infasurf: (A) normalized SLD profile of hLip and hLip + 10% proteins in D_2O, where z is normalized by z_{max} (around 250 Å), such that z_{norm} = 1 at the buffer–air interface and z_{norm} = 0 marks the division between the interfacial structure and the bulk. (B) Normalized SLD profile of Infasurf Ads. and Spr. A schematic for both the hLip + 10% proteins in D_2O and the Infasurf Ads. models is illustrated below each panel, visually representing the SLD information on lipid and protein concentration in each slab. We illustrate the different proteins SP-B and SP-C based on their location from MD simulations.[26,31] Illustrations created in BioRender. Novaes Silva, M. (2025) **https://BioRender.com/46fp3f7**.

The SLD profile of Infasurf Spr. is consistent with that of a monolayer with only negligible multilayer features. Notably, upon spreading, the equilibrium surface tension ($\sim$45 mN m^{-1}) is significantly higher than that of the model system ($\sim$25 mN m^{-1}) at the same interfacial concentration. These results suggest that spreading through an aqueous solution is less effective in forming a stable monolayer, since Marangoni flows that assist in homogeneously distributing the lipids at the interface when spreading from a chloroform solution are absent when spreading from an aqueous solution.[53] We believe that, for the aqueous solution, part of the spread lipid–protein complexes are already assembled and fully hydrated, possibly failing to retain at the interface and, instead, diffusing into the bulk. This likely accounts for both the elevated equilibrium surface tension and the scarce features below the monolayer observed in the SLD profile.

To directly compare the two Infasurf interfaces with the model systems, we normalize the layer thickness z by the size of the multilayer structure where z_{norm} = 1 represents the buffer–air interface and z_{norm} = 0 marks the boundary between the multilayer structure and the bulk, approximately at 250 Å, for both systems. Fig. 7A displays the normalized SLD profile of the hLip and hLip + 10% SPs in D_2O and Fig. 7B, the ones for Infasurf Spr. and Ads. in D_2O. We can infer from the model that the interfacial structure of Infasurf Spr. is predominantly a monolayer, resembling that of the lipid mixture. In contrast, the resulting profile of Infasurf Ads. exhibits multilayer structures, resembling the more complex profile of the 10% SP lipid mixture, even if the distribution is slightly distinct. This supports the idea that, under physiological conditions, proteins may reach higher local concentrations at the interface. Adsorption of bulk aggregates appears to be an effective route to achieve this, as previously proposed.[25] In the SI, we present cryo-TEM images of Infasurf bulk aggregates, which further confirm their similarity to the model system with added protein.

To understand the effect of multilayer structures under dynamic conditions, we show in Fig. 8A the surface stress values as a function of the area variation during the last sigh cycle for the four evaluated systems (hLip, hLip + 10% SPs, Infasurf Spr. and Infasurf Ads. in D_2O).

To mimic physiological lung deformations, we apply an expansion followed by a compression back to the reference area, rather than a compression followed by an expansion. Notably, during breathing, the lungs primarily expand rather than compress[41] – a critical yet often overlooked aspect. Most previous PS studies have focused on measuring interfacial properties under compression.[15,25,54] While such experiments may involve physiologically relevant deformation strains, they can yield misleading values of the stress: compression increases the surface concentration and decreases the surface stress, which is the opposite of the physiological behavior observed during lung expansion. Thus, the x-axis in Fig. 8A represents the percent area expansion relative to the reference area, $A/A_0 - 1$.

Both Infasurf Spr. and the lipid mixture have a similar behavior, where surface stress increases with increasing interfacial area and where no hysteresis is observed between the expansion and compression curves. This is consistent with the SLD profiles (Fig. 7A and B), from which the presence of only a monolayer is inferred. Thus, interfacial properties are likely governed by equilibrium thermodynamics and, at constant temperature, depend only on the surface concentration, Γ ($\sigma_{\alpha\beta}(\Gamma,T)$ in eqn (1)). Consequently, an increase in the interfacial area would reduce the surface concentration, thereby increasing the surface stress, while a re-compression would restore the surface concentration and surface stress back to their initial values. Therefore, the interfacial area appears to modulate surface stress through changes in surface concentration, with no evidence of adsorption/desorption or rheological effects.

Evaluating the surface stress variation of Infasurf Ads. and the lipid mixture with 10% SPs, we identify marked differences. Although both systems have the same initial (equilibrium) surface stress value and have seemingly overall similar multilayer structure, the protein-enriched lipid mixture maintains a relatively constant surface stress throughout expansion. This highlights the role of multilayer structures in facilitating efficient lipid respreading, allowing lipids to flow from the multilayers to the monolayer as the interfacial area increases. In contrast, Infasurf Ads. shows initially a similar behavior to Infasurf Spr. upon expansion, where increasing interfacial area leads to a higher stress. However, the stress plateaus at $A/A_0 - 1 \sim 0.15$, indicating a similar behavior to the lipid mixture with 10% SPs, where lipids are reincorporated into the interfacial monolayer. For Infasurf Ads., newly incorporated material can come either from the multilayered structures, as for the lipids with 10% SPs, or from the bulk. Upon re-compression, the system shows pronounced hysteresis. We attribute this behavior to compressive stresses (σ_e^{iso}) that balance the interfacial tension, thus lowering the total stress. In this case, the newly incorporated material densifies the interface upon compression, forming an interfacial microstructure that can mechanically lower the stress beyond its thermodynamic equilibrium values ($\sim$23 mN m^{-1}).[24]

To highlight the structural differences between Infasurf Ads. and the lipid mixture with 10% proteins upon the breathing protocol, Fig. 8C presents the reflectivity curves for both systems under unstrained and breathing conditions, along with

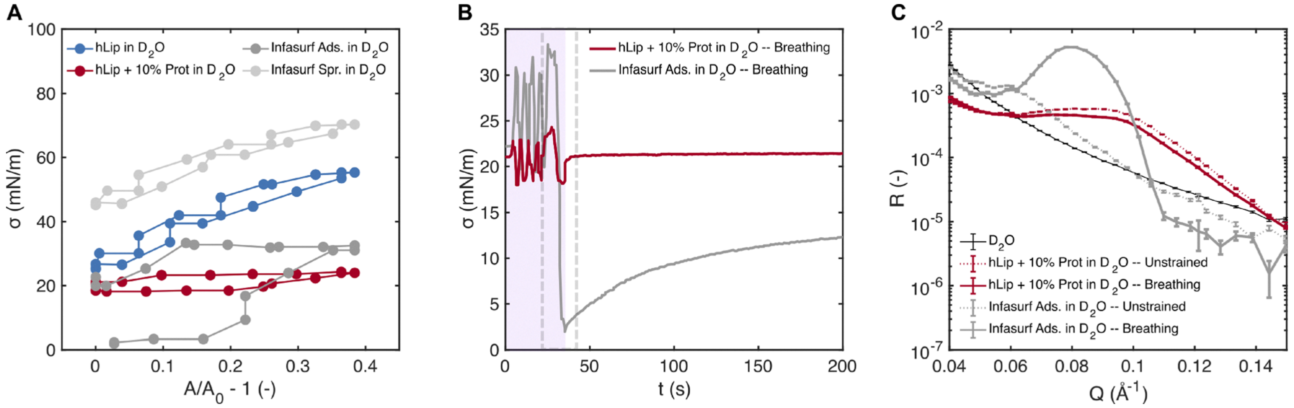

Fig. 8 The effect of the breathing pattern: (A) surface stress (σ) as a function area expansion, defined as $A/A_0 - 1$ for the four systems during a sigh cycle. Upper curves represent the expansion, while bottom ones, the compression. (B) Surface stress as a function of time for hLip + 10% SP-B + 10% SP-C and Infasurf Ads. in D_2O. The purple shaded area indicates the breathing protocol, followed by the waiting time when neutron data is acquired (unshaded). The dashed gray rectangle illustrates the cycle plotted in A. (C) Specular neutron reflectivity (R) as a function of momentum transfer vector (Q) for hLip + 10% SP-B + 10% SP-C and Infasurf Ads. in D_2O under unstrained (dashed lines) and breathing conditions (solid lines) at 36.5 °C. The D_2O reflectivity curve is shown as the black line.

the surface stress values for a representative breathing cycle consisting of four tidal breaths followed by one sigh (Fig. 8B). Fig. 8C shows that the breathing oscillations have a clear impact on the interfacial structure of Infasurf Ads., as illustrated by the pronounced difference between the reflectivity curves before and after the breathing cycles. These differences are most pronounced at high-Q, $\sim$0.1–0.14 Å^{-1} and at the Bragg peak, $\sim$0.08 Å^{-1}. This observation aligns with our previous findings, which showed that sighs play a key role in modifying interfacial structure,[24] and the resulting thermodynamic and mechanical stresses. Specifically, these structural changes were shown to enhance compressive mechanical stresses. This enables the interface to achieve a lower overall surface stress, whereby compressive stresses balance the surface tension upon exhalation.[24] The link between surface stress response and interfacial structure corroborates the hypothesis that σ_e^{iso} is responsible for the hysteresis behavior seen in Fig. 8A.

A similar effect can be seen in Fig. 8B, where Infasurf Ads. exhibits reduced surface stress values following the 3-minute quiescent period after the sigh oscillation, gradually relaxing back to its equilibrium value after cessation of the breathing oscillations. It is worth mentioning that the equilibrium surface stress after the 3-minute period is maintained at a lower value than the equilibrium surface tension of Infasurf. Therefore, we were able to attain and sustain low surface stresses in this system, both hallmarks of pulmonary function.[24] The relaxation behavior and the lower surface stress observed in Fig. 8B associated with structural modifications, shown in Fig. 8C, further confirm the role of compressive stresses in modulating interfacial properties. Other contributions of the surface stress, such as transport-limited phenomena (*i.e.*, adsorption/desorption), are governed by equilibrium thermodynamics, which can change the interfacial concentration, but are not directly related to the formation of an interfacial microstructural network. These findings support the hypothesis that microstructural rearrangements upon compression lower the surface stress and account for the hysteresis behavior observed in Fig. 8A.

On the other hand, the reflectivity curves of the lipid mixture with 10% proteins (Fig. 8C) show only minimal changes before and after the breathing cycles. This suggests that breathing does not significantly alter the interfacial structure. Consistently, no notable relaxation is observed in the surface stress after cessation of breathing oscillations, indicating the absence of metastable changes. As a result, the overall surface stress values remain much higher than those of Infasurf Ads., although the stress variations across the breathing cycle are comparatively smaller, even during sigh expansions.

The striking difference in mechanical response highlights that, while such multilayer structures can enhance interfacial stability and facilitate lipid respreading, they are not sufficient on their own to lower the surface stress. Rather, a continuous bulk supply of lipid–protein aggregates appears essential for that function. To further emphasize the differences in the mechanical response, we show in Fig. 9 the surface stress for the first cycles of the breathing protocol.

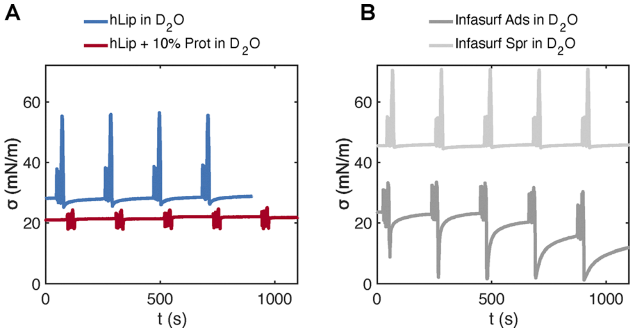

Fig. 9 Structure-rheology coupling: (A) surface stress (σ) as a function of time for the lipid mixture (blue line) and lipid mixture with 10% proteins (red line) in D_2O, representing the first cycles of the breathing protocol with interspersed sighs. (B) Surface stress (σ) as a function of time for Infasurf Spr. (light gray line) and Infasurf Ads. (dark gray line), again for the first cycles of the sigh breathing protocol.

For both the lipid mixture and the 10% protein system (Fig. 9A), the behavior appears to be governed by equilibrium thermodynamics, where increasing interfacial areas lead to higher surface stresses. The protein-added system has smaller stress variations seemingly due to the efficient lipid respreading through the multilayer structures modulated by the SPs. Additionally, no notable relaxation is observed at the end of the breathing cycle. Infasurf Spr. (Fig. 9B) has a similar behavior as the lipid mixture, but it achieves higher surface stress values. On the other hand, Infasurf Ads. (Fig. 9B) shows a markedly different response, achieving lower surface stresses and with gradual changes in relaxation behavior over the cycles. As previously reported, a few sigh cycles are necessary to precondition the interface and induce compressive stresses.[24] Therefore, there should be a gradual change in the overall surface stress over the initial cycles. Indeed, this is observed for Infasurf Ads., where there is a marked difference in both surface stress values and relaxation times over the first five cycles. Notably, the second sigh cycle effectively reduces the surface stress, consistent with previous findings.[24] Additionally, the relaxation time during the 3-minute undisturbed period increases progressively with each cycle, suggesting the system approaches a metastable state. This physiologically relevant state is not achieved for any of the other evaluated systems. All other samples maintain near identical surface stress values throughout the breathing cycles. In addition, no significant relaxation can be observed during the 3-minute period, even for the lipid mixture with 10% proteins, which has relevant multilayer structures.

These findings challenge classical views that attribute surfactant function primarily to the presence of interfacial multilayers. While protein-enriched multilayers can stabilize the interface and support lipid respreading, they do not by themselves enable the dynamic stress regulation observed in the lung. Instead, our data demonstrate that continuous adsorption from a bulk lipid–protein reservoir, as seen in Infasurf under physiological-like conditions, is critical for achieving and maintaining low surface stresses during breathing. This capacity for dynamic structural remodeling, modulated by breathing maneuvers such as sighs, emerges as a defining feature of functional pulmonary surfactant systems, but of course it can be convoluted with transport phenomena and thermodynamic effects.

Conclusions

This study aims to resolve key questions regarding the structural determinants of pulmonary surfactant function. While protein-enriched multilayers have been proposed as reservoirs for lipid respreading, our findings show that their formation alone is not sufficient to achieve a low surface stress under relevant dynamic conditions. Using neutron reflectometry (*in situ*) and cryo-TEM (*ex situ*), we demonstrate that high local concentrations of SP-B and SP-C are required to stabilize multilayers beneath the interface. However, only the clinical surfactant Infasurf, capable of sustaining bulk lipid–protein adsorption, exhibits the dynamic interfacial restructuring needed to lower the surface stress during breathing cycles. These results highlight that surfactant function arises not solely from static multilayer architecture, but also from its ability to undergo structural remodeling under unsteady deformations, as during breathing. Functional performance thus seems to rely on a combined mechanism: multilayer formation enabled by proteins, and continuous interfacial replenishment from the bulk. This has important implications for understanding surfactant failure in disease and for designing more effective replacement therapies.

Author contributions

Conceptualization, M. C. N. S., A. C., M. R. H., J. P. G. and J. V.; methodology, M. C. N. S., A. C., K. P., P. S. P., P. G., J. P. G., N. J. W. and J. V., software, K. P. and P. S. P.; validation, M. C. N. S., A. C. and M. R. H.; formal analysis, M. C. N. S. and B. R. T.; investigation, M. C. N. S., A. C., M. R. H., B. R. T., K. P., J. T. and P. S. P.; resources, J. V., N. J. W., J. P. G., M. A. R.; data curation, M. C. N. S.; writing – original draft, M. C. N. S.; writing – review & editing, M. C. N. S., M. R. H. and J. V.; visualization, M. C. N. S.; supervision, M. R. H. and J. V.; funding acquisition, J. V.

Conflicts of interest

There are no conflicts to declare.

Data availability

The data supporting this article have been included as part of the supplementary information (SI) and in the data repository **https://doi.org/10.3929/ethz-b-000743121** and are publicly available as of the date of publication. Supplementary information is available and provide a slab illustration for neutron reflectivity model fits, model fitting parameters, uncertainty plots for model fitting, an alternative model fit, reflectivity curves of Infasurf, additional cryo-TEM images and individual bilayer thickness for the lipid mixture and lipid mixture with SP-C. See DOI: **https://doi.org/10.1039/d5sm00785b**.

Acknowledgements

We acknowledge neutron beamtime from the ILL Neutron Facility (DOI: **https://doi.org/10.5291/ILL-DATA.9-13-1109**). We would like to thank Dr Kirill ''Sleepy'' Feldman for his help. We acknowledge ScopeM and Dr Bilal Qureshi (ETH Zürich) on their support and assistance in Cryo-TEM experiments. Figure sketches were created using BioRender. Novaes Silva, M. (2025) **https://BioRender.com/hxn8d04**, Novaes Silva, M. (2025) **https://BioRender.com/6nrj1iz** and Novaes Silva, M. (2025) **https://BioRender.com/46fp3f7**. M. R. H. was funded by the ''Proyectos de Investigación Talento Joven UNED 2024''. M. R. H., J. T., and M. A. R. were supported by grants no. PID2020-117080RB-C54 and PID2023-147948OB-C33, financed by Spanish Ministerio de Ciencia, Innovación y Universidades (MCIU), the Agencia Estatal de Investigación (AEI, **https://doi.org/10.13039/501100011033**), and the European Social Fund Plus (FSE+). P. S. P. acknowledges the MICINN-ILL postdoc program for supporting his stay at ILL. N. J. W., B. R. T. and K. P. acknowledge financial support for this work from the U.S. National Institute of Standards and Technology Center for Neutron Research awards # 70NANB17H302, 70NANB20H133 and 70NANB23H227.

Notes and references

1 M. Chavarha, R. W. Loney, K. Kumar, S. B. Rananavare and S. B. Hall, *Langmuir*, 2012, **28**, 16596–16604.

2 S. Han and R. K. Mallampalli, *Ann. Am. Thorac. Soc.*, 2015, **12**, 765–774.

3 W. Bernhard, S. Hoffmann, H. Dombrowsky, G. A. Rau, A. Kamlage, M. Kappler, J. J. Haitsma, J. Freihorst, H. von der Hardt and C. F. Poets, *Am. J. Respir. Cell Mol. Biol.*, 2001, **25**, 725–731.

4 E. Parra and J. Pérez-Gil, *Chem. Phys. Lipids*, 2015, **185**, 153–175.

5 N. Sever, G. Milicic, N. O. Bodnar, X. Wu and T. A. Rapoport, *Mol. Cell*, 2021, **81**, 49–66.e8.

6 M. Chavarha, R. W. Loney, S. B. Rananavare and S. B. Hall, *Biophys. J.*, 2015, **109**, 95–105.

7 M. A. Oosterlaken-Dijksterhuis, H. P. Haagsman, L. M. G. Van Golde and R. A. Demel, *Biochemistry*, 1991, **30**, 8276–8281.

8 D. Schürch, O. L. Ospina, A. Cruz and J. Pérez-Gil, *Biophys. J.*, 2010, **99**, 3290–3299.

9 J. Bernardino de la Serna, R. Vargas, V. Picardi, A. Cruz, R. Arranz, J. M. Valpuesta, L. Mateu and J. Pérez-Gil, *Faraday Discuss.*, 2013, **161**, 535–548.

10 N. Hobi, M. Giolai, B. Olmeda, P. Miklavc, E. Felder, P. Walther, P. Dietl, M. Frick, J. Pérez-Gil and T. Haller, *Biochim. Biophys. Acta, Mol. Cell Res.*, 2016, **1863**, 2124–2134.

11 J. Castillo-Sánchez, A. Cruz and J. Pérez-Gil, *Arch. Biochem. Biophys.*, 2021, **703**, 108850.

12 F. Bringezu, J. Ding, G. Brezesinski, A. J. Waring and J. A. Zasadzinski, *Langmuir*, 2002, **18**, 2319–2325.

13 B. Olmeda, B. García-Álvarez, M. J. Gómez, M. Martínez-Calle, A. Cruz and J. Pérez-Gil, *FASEB J.*, 2015, **29**, 4236–4247.

14 M. Martinez-Calle, M. Prieto, B. Olmeda, A. Fedorov, L. M. Loura and J. Pérez-Gil, *Biochim. Biophys. Acta, Biomembr.*, 2020, **1862**, 183216.

15 M. Martínez-Calle, E. Parra-Ortiz, A. Cruz, B. Olmeda and J. Pérez-Gil, *J. Mol. Biol.*, 2021, **433**, 166749.

16 K. Bouchoris and V. Bontozoglou, *Colloids Surf., A*, 2021, **624**, 126839.

17 A. K. Sachan and J. A. Zasadzinski, *Proc. Natl. Acad. Sci. U. S. A.*, 2018, **115**, E134–E143.

18 S. Baoukina and D. P. Tieleman, *Biophys. J.*, 2011, **100**, 1678–1687.

19 E. Keating, Y. Y. Zuo, S. M. Tadayyon, N. O. Petersen, F. Possmayer and R. A. Veldhuizen, *Biochim. Biophys. Acta, Biomembr.*, 2012, **1818**, 1225–1234.

20 A. K. Sachan, R. K. Harishchandra, C. Bantz, M. Maskos, R. Reichelt and H.-J. Galla, *ACS Nano*, 2012, **6**, 1677–1687.

21 F. Possmayer, Y. Y. Zuo, R. A. W. Veldhuizen and N. O. Petersen, *Chem. Rev.*, 2023, **123**, 13209–13290.

22 A. Alicke, S. Simon, J. Sjoblom and J. Vermant, *Langmuir*, 2020, **36**, 14942–14959.

23 E. Hermans, M. Bhamla, P. Kao, G. Fuller and J. Vermant, *Soft Matter*, 2015, **11**, 8048–8057.

24 M. C. Novaes-Silva, M. Rodríguez-Hakim, B. R. Thompson, N. J. Wagner, E. Hermans, L. J. Dupont and J. Vermant, *Sci. Adv.*, 2025, **11**(39), eadx6034.

25 L. Xu, Y. Yang and Y. Y. Zuo, *Biophys. J.*, 2020, **119**, 756–766.

26 J. Liekkinen, G. Enkavi, M. Javanainen, B. Olmeda, J. Pérez-Gil and I. Vattulainen, *J. Mol. Biol.*, 2020, **432**, 3251–3268.

27 J. Liekkinen, A. Olzynska, L. Cwiklik, J. Bernardino de la Serna, I. Vattulainen and M. Javanainen, *Langmuir*, 2023, **39**, 4338–4350.

28 S. Yu and F. Possmayer, *J. Lipid Res.*, 2003, **44**, 621–629.

29 B. Piknova, V. Schram and S. Hall, *Curr. Opin. Struct. Biol.*, 2002, **12**, 487–494.

30 J. Crane and S. Hall, *Biophys. J.*, 2001, **80**, 1863–1872.

31 R. W. Loney, S. Panzuela, J. Chen, Z. Yang, J. R. Fritz, Z. Dell, V. Corradi, K. Kumar, D. P. Tieleman and S. B. Hall, *et al.*, *J. Phys. Chem. B*, 2020, **124**, 6763–6774.

32 A. Collada, J. Carrascosa-Tejedor, P. Sánchez-Puga, A. Liguori, P. Gutfreund, A. Santamaría, J. C. Castillo-Sánchez, A. Maestro, A. Cruz and J. Pérez-Gil, *J. Colloid Interface Sci.*, 2026, **701**, 138769.

33 J. Pérez-Gil, A. Cruz and C. Casals, *Biochim. Biophys. Acta*, 1993, **1168**(3), 261–270.

34 Y. S. Tein, B. R. Thompson, C. Majkrzak, B. Maranville, D. Renggli, J. Vermant and N. J. Wagner, *Rev. Sci. Instrum.*, 2022, **93**, 093903.

35 S. Q. Choi, S. Steltenkamp, J. A. Zasadzinski and T. M. Squires, *Nat. Commun.*, 2011, **2**, 312.

36 E. Hermans and J. Vermant, *Soft Matter*, 2014, **10**, 175–186.

37 R. Campbell, H. Wacklin, I. Sutton, R. Cubitt and G. Fragneto, *Eur. Phys. J. Plus*, 2011, **126**, 107.

38 D. Follows, F. Tiberg, R. Thomas and M. Larsson, *Biochim. Biophys. Acta, Biomembr.*, 2007, **1768**, 228–235.

39 P. Gutfreund, T. Saerbeck, M. A. Gonzalez, E. Pellegrini, M. Laver, C. Dewhurst and R. Cubitt, *J. Appl. Crystallogr.*, 2018, **51**, 606–615.

40 D. Thomas, J. Marriott, R. Vadlamudi, B. Efendie and L. Maine, in *Clinical Pharmacy Education, Practice and Research*, ed. D. Thomas, Elsevier, 2019.

41 P. Quanjer, G. Tammeling, J. Cotes, O. Pedersen, R. Peslin and J.-C. Yernault, *Eur. Respir. J.*, 1993, **6**, 5–40.

42 B. Kirby, P. Kienzle, B. Maranville, N. Berk, J. Krycka, F. Heinrich and C. Majkrzak, *Curr. Opin. Colloid Interface Sci.*, 2012, **17**, 44–53.

43 W. Fullagar, S. Holt and I. Gentle, *Biophys. J.*, 2008, **95**, 4829–4836.

44 J. A. Vrugt, C. ter Braak, C. Diks, B. A. Robinson, J. M. Hyman and D. Higdon, *Int. J. Nonlinear Sci. Numer. Simul.*, 2009, **10**, 273–290.

45 D. Danino, *Curr. Opin. Colloid Interface Sci.*, 2012, **17**, 316–329.

46 K. A. Taylor and R. M. Glaeser, *J. Struct. Biol.*, 2008, **163**, 214–223.

47 W. Wiese and W. Helfrich, *J. Phys.: Condens. Matter*, 1990, **2**, SA329.

48 S. Baoukina, L. Monticelli, H. J. Risselada, S. J. Marrink and D. P. Tieleman, *Proc. Natl. Acad. Sci. U. S. A.*, 2008, **105**, 10803–10808.

49 W. Rawicz, K. Olbrich, T. McIntosh, D. Needham and E. Evans, *Biophys. J.*, 2000, **79**, 328–339.

50 S. Taneva and K. M. Keough, *Biophys. J.*, 1994, **66**, 1137–1148.

51 A. Cruz, L. Vázquez, M. Vélez and J. Pérez-Gil, *Biophys. J.*, 2004, **86**, 308–320.

52 O. Blanco and J. Pérez-Gil, *Eur. J. Pharmacol.*, 2007, **568**, 1–15.

53 G. Fuller and J. Vermant, *Annu. Rev. Chem. Biomol. Eng.*, 2012, **3**, 519–543.

54 C. Ciutara, S. Iasella, B. Huang, S. Barman and J. Zasadzinski, *Proc. Natl. Acad. Sci. U. S. A.*, 2023, **120**, e2309900120.